J|A|C|S ARTICLES

Published on Web 09/14/2010

Structure and Valency of a Cobalt−Phosphate Water Oxidation Catalyst Determined by in Situ X-ray Spectroscopy

Matthew W. Kanan,[†,§] Junko Yano,[‡] Yogesh Surendranath,[†] Mircea Dincă,[†] Vittal K. Yachandra,*[,‡] and Daniel G. Nocera*[,†]

Department of Chemistry, 6-335, Massachusetts Institute of Technology, Cambridge, Massachusetts 02139, and Physical Bioscience Division, Lawrence Berkeley National Laboratory, Berkeley, California 94720

Received April 4, 2010; E-mail: vkyachandra@lbl.gov (V.K.Y.); nocera@mit.edu (D.G.N.)

Abstract: A water oxidation catalyst generated via electrodeposition from aqueous solutions containing phosphate and Co^{2+} (Co−Pi) has been studied by in situ X-ray absorption spectroscopy. Spectra were obtained for Co−Pi films of two different thicknesses at an applied potential supporting water oxidation catalysis and at open circuit. Extended X-ray absorption fine structure (EXAFS) spectra indicate the presence of bis-oxo/hydroxo-bridged Co subunits incorporated into higher nuclearity clusters in Co−Pi. The average cluster nuclearity is greater in a relatively thick film (∼40−50 nmol Co ions/cm^2) deposited at 1.25 V vs NHE than in an extremely thin film (∼3 nmol Co ions/cm^2) deposited at 1.1 V. X-ray absorption near edge structure (XANES) spectra and electrochemical data support a Co valency greater than 3 for both Co−Pi samples when catalyzing water oxidation at 1.25 V. Upon switching to open circuit, Co−Pi undergoes a continuous reduction due to residual water oxidation catalysis, as indicated by the negative shift of the edge energy. The rate of reduction depends on the average cluster size. On the basis of structural parameters extracted from fits to the EXAFS data of Co−Pi with two different thicknesses and comparisons with EXAFS spectra of Co oxide compounds, a model is proposed wherein the Co oxo/hydroxo clusters of Co−Pi are composed of edge-sharing CoO_6 octahedra, the structural motif found in cobaltates. Whereas cobaltates contain extended planes of CoO_6 octahedra, the Co−Pi clusters are of molecular dimensions.

Introduction

Converting water to O_2 and H_2 is the central chemistry of energy conversion processes that store renewable sources in the form of chemical fuels.[1,2] This overall transformation can be accomplished using electrocatalysts to mediate two separate half reactions: the two-electron reduction of water to H_2 and the four-electron oxidation of water to O_2. Different configurations are possible for the integration of solar energy input to the electrocatalysts. In the most straightforward construct, water-splitting electrocatalysts are powered by a separate photovoltaic component.[3−5] Alternatively, the tasks of light absorption and catalysis can be combined in a photoelectrode that effects H_2 and/or O_2 production upon illumination in a suitable electrolyte.[6] A variety of water-splitting devices incorporating one or more photoelectrodes may be constructed.[7−10]

[†] Massachusetts Institute of Technology.
[‡] Lawrence Berkeley National Laboratory.
[§] Current Address: Department of Chemistry, Stanford University, Stanford, CA 94305-5080.

(1) Nocera, D. G. *Inorg. Chem.* **2009**, *48*, 10001–10007.
(2) Lewis, N. S.; Nocera, D. G. *Proc. Natl. Acad. Sci. U.S.A.* **2006**, *103*, 15729–15735.
(3) Grimes, C. A.; Varghese, O. K.; Ranjan, S. In *Light, Water, Hydrogen*; Springer: New York, 2008.
(4) Turner, J.; Sverdrup, G.; Mann, M. K.; Maness, P.; Kroposki, B.; Ghirardi, M.; Evans, R. J.; Blake, D. *Int. J. Energy Res.* **2008**, *32*, 379–407.
(5) Licht, S.; Wang, B.; Mukerji, S.; Soga, T.; Umeno, M.; Tributsch, H. *Int. J. Hydrogen Energy* **2001**, *26*, 653–659.
(6) Osterloh, F. E. *Chem. Mater.* **2008**, *20*, 35–54.
(7) Weber, M. F.; Dignam, M. J. *J. Electrochem. Soc.* **1984**, *131*, 1258–1265.
(8) Bard, A. J.; Fox, M. A. *Acc. Chem. Res.* **1995**, *28*, 141–145.
(9) Khaselev, O.; Turner, J. A. *Science* **1998**, *280*, 425–427.
(10) Brillet, J.; Cornuz, M.; Le Formal, F.; Yum, J.; Grätzel, M.; Sivula, K. *J. Mater. Res.* **2010**, *25*, 17–24.
(11) Trasatti, S. In *Electrochemistry of Novel Materials*; Lipkowski, J., Ross, P. N., Eds.; VCH: New York, 1994.
(12) Tarasevich, M. R.; Efremov, B. N. In *Electrodes of Conductive Metal Oxides*; Elsevier: Amsterdam, 1980.
(13) Trasatti, S. *Electrochim. Acta* **1984**, *29*, 1503–1512.
(14) Singh, R. N.; Pandey, J. P.; Singh, N. K.; Lal, B.; Chartier, P.; Koenig, J. F. *Electrochim. Acta* **2000**, *45*, 1911–1919.
(15) Di Blasi, A.; D'Urso, C.; Baglio, V.; Antonucci, V.; Arico, A. S.; Ornelas, R.; Matteucci, F.; Orozco, G.; Beltran, D.; Meas, Y.; Arriaga, L. G. *J. Appl. Electrochem.* **2009**, *39*, 191–196.
(16) Marshall, A.; Borresen, B.; Hagen, G.; Tsypkin, M.; Tunold, R. *Energy* **2007**, *32*, 431–436.
(17) Gibson, T. L.; Kelly, N. A. *Int. J. Hydrogen Energy* **2008**, *33*, 5931–5940.
(18) Kanan, M. W.; Nocera, D. G. *Science* **2008**, *321*, 1072–1075.
(19) Lutterman, D. A.; Surendranath, Y.; Nocera, D. G. *J. Am. Chem. Soc.* **2009**, *131*, 3838–3839.
(20) Zhong, D. K.; Gamelin, D. R. *J. Am. Chem. Soc.* **2010**, *132*, 4202–4207.
(21) Kanan, M. W.; Surendranath, Y.; Nocera, D. G. *Chem. Soc. Rev.* **2009**, *38*, 109–114.
(22) Zhong, D. K.; Sun, J.; Inumaru, H.; Gamelin, D. R. *J. Am. Chem. Soc.* **2009**, *131*, 6086–6087.
(23) Steinmiller, E. M. P.; Choi, K. *Proc. Natl. Acad. Sci. U.S.A.* **2009**, *106*, 20633–20636.
(24) Surendranath, Y.; Dincă, M.; Nocera, D. G. *J. Am. Chem. Soc.* **2009**, *131*, 2615–2620.
(25) Risch, M.; Khare, V.; Zaharieva, I.; Gerencser, L.; Chernev, P.; Dau, H. *J. Am. Chem. Soc.* **2009**, *131*, 6936–6937.

10.1021/ja1023767

Conductive metal oxides have been studied and employed as water oxidation catalysts in electrolyzers for many decades.[3,11−13] First-row metal oxides such as Co- or Ni-containing spinels and perovskites are typically employed in alkaline electrolyzers that operate in concentrated KOH solutions,[14] while metal oxides such as RuO_2 and IrO_2 are typically employed in proton-exchange membrane (PEM) electrolyzers that operate under highly acidic conditions.[15,16] Electrolysis at the pH extremes is a remarkably robust and efficient process with electric-to-chemical energy conversion efficiencies in the range of 60−90%, depending on the precise conditions employed.[3] Furthermore, overall light-to-chemical (H_2) energy conversion efficiencies of up to 12% have been reported for systems consisting of photovoltaic cells connected to a conventional PEM electrolyzer.[17] Despite these impressive efficiencies, distributed solar energy storage via systems of this sort remains prohibitively expensive. One possible path to lowering the cost and the barrier to proliferation of solar-to-hydrogen energy storage is to develop electrolysis technologies that operate under benign conditions. Such electrolyzers would not require expensive membranes and catalysts, or the high balance of systems costs that accompany the operation of electrolysis in harsh environments.

We recently described a water oxidation catalyst, Co−Pi, that deposits on electrode surfaces upon application of anodic potentials in neutral phosphate-buffered water containing Co^{2+}.[18] Co−Pi exhibits high activity under benign conditions and has the ability to undergo repair[19] upon cycling between applied and open circuit potentials (OCP). In addition, Co−Pi is readily interfaced with a variety of conductive and semiconductive surfaces via either electrodeposition[20−22] or photodeposition[23] processes. This attribute makes Co−Pi a particularly attractive candidate for the development of catalyst-functionalized photoelectrodes that drive direct water oxidation upon illumination.

Elucidation of Co−Pi's chemical structure and valency during catalysis is an essential step toward gaining a mechanistic understanding of water oxidation. Moreover, structural insights provide a starting point for the construction of structure−activity relationships in water oxidation catalysts prepared via electrodeposition, potentially informing the development of more active catalysts. The construction of such structure−activity relationships, however, is impeded by the amorphous nature of the Co−Pi catalyst within the resolution of powder X-ray diffraction and transmission electron microscopy.[18,24] In the absence of crystallites, X-ray absorption spectroscopy (XAS) provides a powerful tool for the elucidation of local structure. A recent XAS study of Co−Pi was reported wherein the catalyst was quickly frozen after electrodeposition and spectra were collected ex situ.[25] This study proposed a corner-sharing Co−oxo cubane architecture for Co−Pi. Here we describe XAS of Co−Pi during catalytic turnover for both extremely thin films of approximate monolayer thickness and somewhat thicker films with >10× more material. Our in situ experiments provide insight into Co valency during catalysis and valency changes when an applied potential is removed. In addition, our studies lead us to a structural model that differs from that of the previous study. On the basis of structural parameters extracted from fits to the EXAFS data of Co−Pi with two different thicknesses and comparisons with EXAFS spectra of Co oxide compounds, we propose that Co−Pi consists of Co oxo/hydroxo clusters of molecular dimensions. The clusters consist of edge-sharing CoO_6 octahedra, the same structural motif found in the extended planes of the cobaltates. However, unlike cobaltates, which are stable to water at Co valencies ≥3.4, Co−Pi is an active water oxidation catalyst when the Co valency is raised above 3. These results suggest that the high catalytic activity of Co−Pi may result from the molecular nature of the constituent Co−oxo/hydroxo clusters.

Experimental Section

Model Compounds. Crystalline CoO(OH) was prepared by annealing β-$Co(OH)_2$ in a flow of O_2 according to a previously published procedure,[26] and its identity was verified by powder X-ray diffraction. CoO and Co_3O_4 were purchased from Aldrich.

Catalyst Electrodeposition for in Situ XAS. Co−Pi catalyst samples were electrodeposited from freshly prepared 0.5 mM $Co(NO_3)_2$ solutions in either 0.1 M potassium phosphate buffer, pH 7.0 (KPi), or 0.1 M sodium phosphate buffer, pH 7.0 (NaPi), just prior to collection of XAS spectra. The electrochemical cell consisted of two compartments separated by a glass frit. One compartment contained a flat glass wall, out of which a circular opening 1.5 cm in diameter was cut. Using epoxy glue, a 2 cm × 3.3 cm piece of ITO-coated polyethylene terephthalate (ITO-PET, Kintec Company) was attached to the inside of this wall with the ITO side facing inward. The ITO layer (~0.15 μm) served as the working electrode upon which the catalyst was deposited. Connection of the ITO to the potentiostat was made via an alligator clip. The X-ray transparency of the PET layer and relatively thin ITO layer enabled XAS spectra to be collected through the circular opening under the operating conditions. A Ag/AgCl reference electrode and a Pt wire counterelectrode were used for all experiments. The compartment to which the ITO-PET was attached was fitted with a Teflon cap containing a hole through which the reference electrode was placed. This setup ensured a reproducible spacing between the reference electrode and working electrode between experiments.

(26) Amatucci, G. G.; Tarascon, J. M.; Larcher, D.; Klein, L. C. *Solid State Ionics* **1996**, *84*, 169–180.
(27) Newville, M. *J. Synchrotron Rad.* **2001**, *8*, 322–324.
(28) Rehr, J. J.; Albers, R. C. *Rev. Mod. Phys.* **2000**, *72*, 621–654.
(29) McAlpin, J. G.; Surendranath, Y.; Dincă, M.; Stich, T. A.; Stoian, S. A.; Casey, W. H.; Nocera, D. G.; Britt, R. D. *J. Am. Chem. Soc.* **2010**, *132*, 6882–6883.
(30) Delaplane, R. G.; Ibers, J. A.; Ferraro, J. R.; Rush, J. J. *J. Chem. Phys.* **1969**, *50*, 1920–1928.
(31) Ama, T.; Rashid, M. M.; Yonemura, T.; Kawaguchi, H.; Yasui, T. *Coord. Chem. Rev.* **2000**, *198*, 101–116.
(32) Poltavets, V. V.; Croft, M.; Greenblatt, M. *Phys. Rev. B: Condens. Mater. Phys.* **2006**, *74*, 125103/1−8.
(33) Chakrabarty, R.; Bora, S. J.; Das, B. K. *Inorg. Chem.* **2007**, *46*, 9450–9462.
(34) Dimitrou, K.; Brown, A. D.; Concolino, T. E.; Rheingold, A. L.; Christou, G. *Chem. Commun.* **2001**, 1284–1285.
(35) Dimitrou, K.; Folting, K.; Streib, W. E.; Christou, G. *J. Am. Chem. Soc.* **1993**, *115*, 6432–6433.
(36) Beattie, J. K.; Hambley, T. W.; Klepetko, J. A.; Masters, A. F.; Turner, P. *Polyhedron* **1998**, *17*, 1343–1354.
(37) Chakrabarty, R.; Sarmah, P.; Saha, B.; Chakravorty, S.; Das, B. K. *Inorg. Chem.* **2009**, *48*, 6371–6379.
(38) Yin, Q.; Tan, J. M.; Besson, C.; Geletti, Y. V.; Musaev, D. G.; Kuznetsov, A. E.; Luo, Z.; Hardcastle, K. I.; Hill, C. L. *Science* **2010**, *328*, 342–345.
(39) Chivot, J.; Mendoza, L.; Mansour, C.; Pauporté, T.; Cassir, M. *Corros. Sci.* **2008**, *50*, 62–69.
(40) McClintock, L. F.; Blackman, A. G. *Chem. Asian J.* **2010**, *5*, 756–758.
(41) Brunschwig, B. S.; Chou, M. H.; Creutz, C.; Ghosh, P.; Sutin, N. *J. Am. Chem. Soc.* **1983**, *105*, 4832–4833.
(42) Takada, K.; Fukuda, K.; Osada, M.; Nakai, I.; Izumi, F.; Dilanian, R. A.; Kato, K.; Takata, M.; Sakurai, H.; Takayama-Muromachi, E.; Sasaki, T. *J. Mater. Chem.* **2004**, *14*, 1448–1453.
(43) Sakurai, H.; Tsujii, N.; Suzuki, O.; Kitazawa, H.; Kido, G.; Takada, K.; Sasaki, T.; Takayama-Muromachi, E. *Phys. Rev. B: Condens. Mater. Phys.* **2006**, *74*, 092502/1−4.
(44) Sakurai, H.; Osada, M.; Takayama-Muromachi, E. *Chem. Mater.* **2007**, *19*, 6073–6076.
(45) Ren, Z.; Luo, J.; Xu, Z.; Cao, G. *Chem. Mater.* **2007**, *19*, 4432–4435.

The "bulk" and "surface" Co−Pi catalyst samples were electrodeposited from freshly prepared 0.5 mM $Co(NO_3)_2$ solutions in 0.1 M potassium phosphate buffer, pH 7.0 (KPi). Deposition of bulk Co−Pi was carried out at 1.25 V (all voltages are reported with respect to the Normal Hydrogen Electrode, NHE) until 60 mC/cm^2 of charge (0.26 C) was passed. The solution containing Co^{2+} was then removed from the working compartment of the cell and this compartment was rinsed three times and refilled with Co^{2+}-free buffer. Surface Co−Pi was electrodeposited at 1.1 V (NHE) until 1.6 mC of charge was passed (300 μC/cm^2). Because some material is lost during a rinse, only one rinse was used for the surface Co−Pi sample.

An upper limit of the amount of Co deposited per electrode surface area for surface Co−Pi (3 nmol/cm^2) was calculated by assuming that all charge was accounted for by $Co^{2+/3+}$ oxidation and that all oxidized Co was deposited. To estimate the amount of Co ions in bulk Co−Pi, a film was prepared independently at 1.25 V on an ITO-coated glass slide (Sigma, 8−12 Ω/sq) with the same amount of charge per electrode surface area and a cyclic voltammogram (CV) was obtained of the resulting film (Figure S1, Supporting Information). This CV was compared to the CVs of a series of standard films prepared by deposition at low potential for which an upper limit for the amount of Co deposited can be determined by the charge passed in the deposition. The CV of the film deposited at 1.25 V matched that of a film prepared in a 4.6 mC/cm^2 deposition at low potential. We therefore estimate 40−50 nmol/cm^2 as the amount of Co ions in bulk Co−Pi.

XAS Data Acquisition. X-ray absorption spectra were collected at the Stanford Synchrotron Radiation Lightsource (SSRL) on beamlines 7−3 and 9−3 at an electron energy of 3.0 GeV with an average current of 90 mA. The radiation was monochromatized by a Si(220) double-crystal monochromator. The intensity of the incident X-ray (I_0) was monitored by an N_2-filled ion chamber in front of the sample. The data were collected as fluorescence excitation spectra with a Ge 30 element detector (Canberra). Energy was calibrated by the rising edge position of Co foil (7709.5 eV) for Co XAS. The X-ray flux at 7800 eV measured at I_0 was about 8×10^9 photons s^{-1} mm^{-2}. Spectra were measured at room temperature.

Acquisition of XAS spectra was initiated immediately following Co−Pi electrodeposition and rinsing of the working compartment. For bulk Co−Pi, a potential of 1.25 V was applied to the working electrode for 200 s and the cell was then switched to open circuit (OC). One near edge scan was obtained while the open circuit potential (OCP) was measured at 1 s intervals. The cell was then switched back to 1.25 V and four full scans were obtained. A current density ≥40 μA/cm^2 was sustained throughout collection of data at 1.25 V. For surface Co−Pi, 32 full scans were obtained at 1.25 V first, during which time the catalyst sustained a current density ≥3.5 μA/cm^2. The cell was then switched to OC and four near edge scans were obtained. The difference in current densities between bulk and surface Co−Pi at 1.25 V reflects the difference in the amount of catalyst material between the two samples.

Data reduction of the EXAFS spectra was performed using EXAFSPAK (Drs. Graham George and Ingrid Pickering, SSRL). Pre-edge and postedge backgrounds were subtracted from the XAS spectra and the results were normalized with respect to edge height. Background removal in k-space was achieved through a five-domain cubic spline. Curve fitting was performed with Artemis and IFEFFIT software using ab initio calculated phases and amplitudes from the program FEFF 8.2.[27,28] These ab initio phases and amplitudes were used in the EXAFS equation:

$$\chi(k) = S_0^2 \sum_j \frac{N_j}{kR_j^2} f_{\mathrm{eff}_j}(\pi, k, R_j)\, \mathrm{e}^{-2\sigma_j^2 k^2}\, \mathrm{e}^{-2R_j/\lambda_j(k)} \sin(2kR_j + \phi_{ij}(k)) \quad (1)$$

The neighboring atoms to the central atom(s) are divided into j shells, with all atoms with the same atomic number and distance from the central atom grouped into a single shell. Within each shell, the coordination number N_j denotes the number of neighboring atoms in shell j at a distance of R_j from the central atom. $f_{\mathrm{eff}_j}(\pi,k,R_j)$ is the ab initio amplitude function for shell j, and the Debye−Waller term $\mathrm{e}^{-2\sigma_j^2 k^2}$ accounts for damping due to static and thermal disorder in absorber−backscatterer distances. The mean free path term $\mathrm{e}^{-2R_j/\lambda_j(k)}$ reflects losses due to inelastic scattering, where $\lambda_j(k)$ is the electron mean free path. The oscillations in the EXAFS spectrum are reflected in the sinusoidal term, $\sin(2kR_j + \phi_{ij}(k))$ where $\phi_{ij}(k)$ is the ab initio phase function for shell j. S_0^2 is an amplitude reduction factor due to shakeup/shake-off processes at the central atom(s). The EXAFS equation was used to fit the experimental data using N, R, and the EXAFS Debye−Waller factor (σ^2) as variable parameters. For the energy (eV)-to-wave vector (k, Å^{-1}) axis conversion, E_0 was defined as 7720 eV. EXAFS curve-fitting procedures and the estimations of the uncertainty in the parameters from the fits are described in detail in the Supporting Information.

Results

In Situ X-ray Absorption Spectroscopy. Cobalt K-edge X-ray absorption spectroscopy (XAS) was performed on freshly prepared Co−Pi catalysts in situ at open circuit (OC) and during active catalysis. These experiments employed a modified two-compartment electrolysis cell containing an X-ray transparent window, the solution-facing side of which was coated with a thin layer of indium tin oxide (ITO). The ITO served as the working electrode upon which the Co−Pi catalyst was deposited. X-ray absorption was measured as a fluorescence excitation spectrum. This configuration prevented interference from the electrolyte solution or bubbles that formed during catalysis.

XAS spectra reflect the electronic and structural environment of the major metal ion species in a sample. In the case of Co−Pi, the majority of Co ions in a thick film may not be exposed to the electrolyte and therefore may not be able to participate in catalysis. To ensure that XAS spectra were representative of electrolyte-exposed Co−Pi, we sought the lower limit of the amount of electrodeposited Co−Pi that would yield spectra with acceptable signal-to-noise ratios. To prepare these extremely thin samples, electrodepositions from solutions of 0.5 mM Co^{2+} in 0.1 M KPi were carried out at 1.1 V. At this potential, H_2O oxidation activity of the deposited catalyst is minimal, and essentially all of the current can be attributed to $Co^{2+/3+}$ oxidation events. Spectra with acceptable signal-to-noise ratios were obtained with as little as 300 μC/cm^2 of charge passed in a deposition, corresponding to 3 nmol/cm^2 as the upper limit for the amount of Co in the deposited material. For a Co−Co distance of 2.82 Å and hexagonal arrangements of Co ions (vide infra), 3 nmol/cm^2 of Co corresponds to a few monolayers of coverage of Co−Pi. Given the amorphous nature of Co−Pi, this extremely low level of coverage likely ensures that nearly all of the Co−Pi material is exposed to electrolyte during catalysis. Such an extremely thin sample, hereafter referred to as "surface Co−Pi", therefore mimics the surface of a thicker sample.

After the deposition of a surface Co−Pi sample, the working compartment was rinsed and refilled with Co^{2+}-free KPi. A potential of 1.25 V was applied to the catalyst and XAS spectra were collected. Because of the small amount of Co ions in the sample, a total of 32 scans were averaged to yield the spectrum in Figure 1. Sustained currents indicative of water oxidation were observed throughout the course of data collection.

Following data collection at 1.25 V, the cell was switched to OC, and four near edge scans were obtained during which the

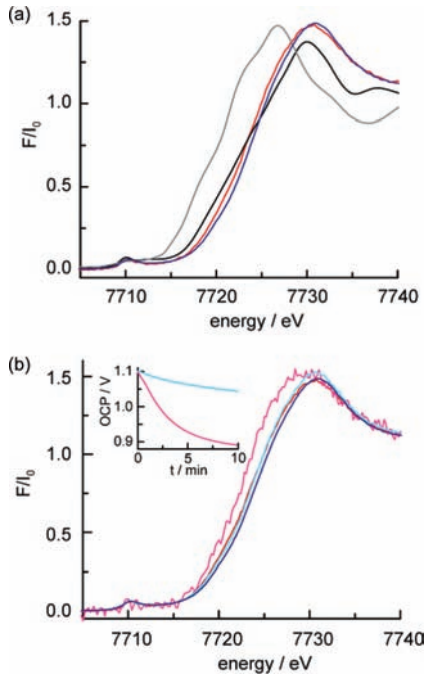

Figure 1. XANES spectra for Co−Pi samples and model compounds: (a) Surface Co−Pi at 1.25 V (red), bulk Co−Pi at 1.25 V (blue), CoO(OH) (black), and CoO (gray). (b) Surface Co−Pi at OCP (magenta) and 1.25 V (red), bulk Co−Pi at OCP (cyan) and 1.25 V (blue). Inset: open circuit potential vs time.

OCP was monitored. Losses of intensity and monotonic shifts to lower edge energies were observed in successive scans. This result is indicative of the formation of Co^{2+} at OCP (vide infra) and concomitant dissolution of surface Co−Pi, a phenomenon that has been detected in ^{57}Co-labeling experiments.[19] This dissolution is reversed during operation of the catalyst, engendering its self-healing properties.

In addition to the surface Co−Pi sample, a thicker sample, hereafter designated as "bulk Co−Pi", was prepared by performing electrodepositions at a higher potential than that used for the preparation of surface Co−Pi. Bulk Co−Pi was prepared at 1.25 V until 60 mC/cm^2 of charge was passed. Because deposition coincides with water oxidation at this potential, the amount of charge passed does not directly indicate the amount of Co^{3+} ions deposited at 1.25 V. However, CV measurements of independently prepared films (Figure S1, Supporting Information) indicate that the Co−Pi sample prepared under these conditions contains approximately 40−50 nmol/cm^2 of Co ions. We note that in previous reports, Co−Pi was typically prepared via electrodeposition at 1.3 V for much longer durations than in the procedure used here for bulk Co−Pi, resulting in much thicker films.[18,19,22,24,25] The preparations are similar, however, in that at 1.25 and 1.3 V deposition coincides with water oxidation catalysis.

After deposition of bulk Co−Pi, the working compartment was rinsed and refilled with Co^{2+}-free electrolyte and a potential of 1.25 V was applied to the electrode for 200 s. The cell was then switched to OC and one near edge scan was collected during which the OCP was monitored. The OCP decayed monotonically from 1.1 to 1.04 V over the 10 min of data collection. Following acquisition of the near edge spectrum at OC, the cell was switched back to 1.25 V. Four full scans were collected at this potential while water oxidation catalysis proceeded. A current density $\geq$40 μA/cm^2 was sustained throughout the course of data collection.

XANES Spectra. The X-ray absorption near edge structure (XANES) spectra for surface Co−Pi and bulk Co−Pi during catalysis at 1.25 V are shown in Figure 1a. Also included are the spectra for solid samples of the Co^{2+} and Co^{3+} oxide model compounds CoO and CoO(OH), respectively. The edges for the Co−Pi samples are approximately 4 eV higher in energy than that of CoO and are much closer to that of CoO(OH). The edge positions observed here are therefore consistent with an average Co valency $\geq$3 for the Co−Pi samples, although it is difficult to determine metal valency based only on XANES spectra due to their sensitivity to geometry and ligand environment. A Co valency $\geq$3 is additionally supported by electrochemical data (vide infra) and recent EPR detection of Co^{4+} in Co−Pi samples.[29] The shapes of the edges for bulk Co−Pi and surface Co−Pi are very similar, and a comparison of the inflection points obtained from the second derivative plots indicates that the edge of the bulk sample is 0.3 eV higher than the edge of the surface sample (Figure S2, Supporting Information). This result is consistent with a greater Co valency in the relatively thick bulk Co−Pi sample compared to the thinner surface Co−Pi sample.

The XANES spectra for bulk Co−Pi and surface Co−Pi at OC are shown in Figure 1b. For comparison, XAS spectra collected on catalyst films held at 1.25 V are shown again. Also shown in Figure 1b are the OCP vs time traces for both samples over the 10 min required to obtain the near edge scan at OC (inset). Importantly, these OCP traces indicate that the spectra do not reflect a Co−Pi catalyst at steady-state. The OCP of bulk Co−Pi exhibits a smooth decay of ~60 mV over the course of data collection, and the OCP of surface Co−Pi exhibits a much more drastic drop of >200 mV. The XANES spectrum of bulk Co−Pi at OC is shifted lower in energy by ~0.3 eV relative to the bulk Co−Pi spectrum at 1.25 V. Successive switching between OC and 1.25 V for bulk Co−Pi reproduces this edge shift. Consistent with the more rapid decay in OCP, the XANES spectrum of surface Co−Pi at OC exhibits a ~1 eV shift to lower energy relative to the corresponding spectrum at 1.25 V. Together, these results indicate a continuous reduction of the Co−Pi catalyst upon switching from a potential sufficient for sustained water oxidation catalysis to OC. A larger fraction of the Co ions in the surface Co−Pi sample are reduced in a given time period relative to the bulk Co−Pi sample.

EXAFS Spectra. The k^3-weighted EXAFS spectra and their Fourier transforms (FT) for surface Co−Pi at 1.25 V, bulk Co−Pi at 1.25 V, and CoO(OH) are shown in Figure 2. In the FT spectra, the abscissa is apparent distance (R'), which is shorter than the actual distance between a given absorber−backscatterer pair of atoms due to a phase shift. Compared with the spectra for CoO and Co_3O_4 (Figure S3, Supporting Information), the EXAFS spectrum for CoO(OH) bears a much stronger resemblance to the spectra of the Co−Pi samples. All three data sets in Figure 2 show two prominent peaks (peaks I and II) in different ratios. These peaks reflect Co−O and Co−Co vectors, respectively, as indicated by the EXAFS fits (vide infra). For CoO(OH), peak II is more intense than peak I, whereas the opposite is true for the Co−Pi samples. Notably, the intensity of peak II is greater for bulk Co−Pi than for surface Co−Pi, reflecting a larger average number of Co−Co vectors per Co ion in bulk Co−Pi compared to surface Co−Pi. The FT for CoO(OH) clearly shows other prominent features in the regions designated as peaks III and IV. These features are consistent with contributions from scattering interactions in outer shells, as expected for the crystalline CoO(OH) sample. Much weaker features are present in the FT for bulk Co−Pi at peaks III and

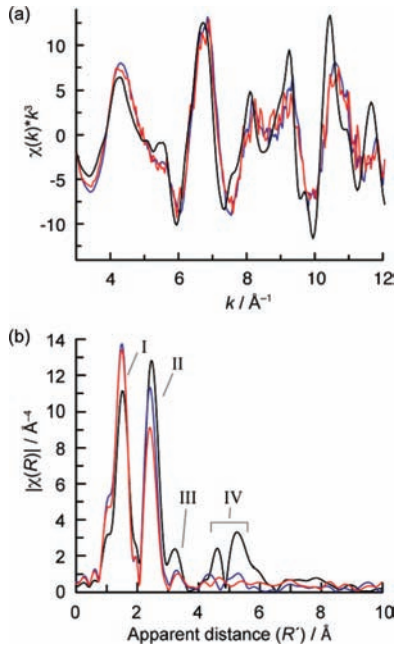

Figure 2. EXAFS spectra and Fourier transforms for Co−Pi and CoO(OH). (a) k^3-weighted EXAFS oscillations for bulk Co−Pi (blue), surface Co−Pi (red), and CoO(OH) (black). (b) Fourier transforms of *k*-space oscillations for bulk Co−Pi (blue), surface Co−Pi (red), and CoO(OH) (black).

Table 1. CoO(OH) EXAFS Fitting Parameters[a]

	R (Å)					
path	XRD	EXAFS[c]	*N*[b]	σ^2 (Å^{-2})[c]	ΔE_0 (eV)[c]	R_f (%)
CoO	1.90	1.90 (0.010)	**6.0**	0.004 (0.001)	1.2 (1.1)	3.4
CoCo	2.85	2.85 (0.008)	**6.0**	0.005 (0.001)		
CoO[d]	3.83	3.78 (0.025)	**6.0**	0.006 (0.003)		
CoCo	4.94	4.98 (0.030)	**6.0**	0.009 (0.003)		
CoCo[e]	5.71	5.76 (0.021)	**6.0**	0.004 (0.001)		

[a] Fitting region: $1 \le R(\text{Å}) \le 6$, $2.88 \le k(\text{Å}^{-1}) \le 11.73$. [b] Bold numbers indicate fixed values. [c] Values in parentheses are uncertainties. See Supporting Information for details. [d] Interlayer interactions. [e] Multiple scattering path, Co−Co−Co.

IV. For surface Co−Pi, only a very small feature at peak III is distinguishable from the background.

Curve-Fitting Analysis. Structural parameters were obtained for surface and bulk Co−Pi by curve fitting the spectra. To aid this analysis, curve fitting was first performed for the spectrum of CoO(OH) (Table 1) for which the crystal structure is known[30] (Figure 3a). An excellent fit to this spectrum was obtained by including backscatterer atoms of five paths up to 5.8 Å away and fixing the number of neighbors in each shell (*N* value) to those determined from the CoO(OH) crystal structure (Figure 3b and Table 1; a complete set of fits is shown in Supporting Information, Table S1). Actual distances (*R*) determined from this fit closely matched the crystallographic distances for the first two shells (peaks I and II) and were within 0.05 Å of these values for outer shells (peaks III and peak IV region) (Table 1). The peak IV region includes a long multiple scattering path (Co−Co−Co) that arises from the linear arrangement of three oxo-bridged Co ions. The value for the damping factor (S_0^2) obtained from this fit, 0.75, was used in the fits for bulk and surface Co−Pi because of the similarity of the spectra of CoO(OH) with those of Co−Pi.

A good fit to the EXAFS spectrum for surface Co−Pi was obtained by including only two absorber−backscatterer pairs

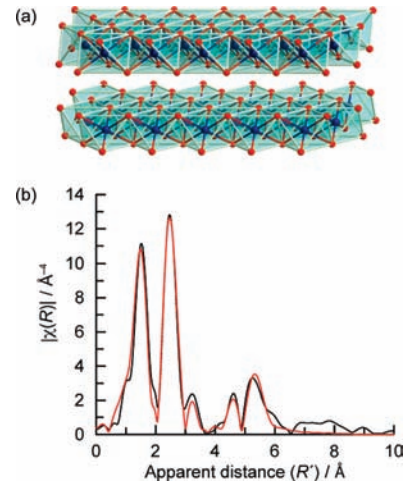

Figure 3. CoO(OH) model compound. (a) X-ray crystal structure of CoO(OH). (b) Fit (red) to the EXAFS spectra (black) in *R*-space. Parameters derived from the fit are given in Table 1.

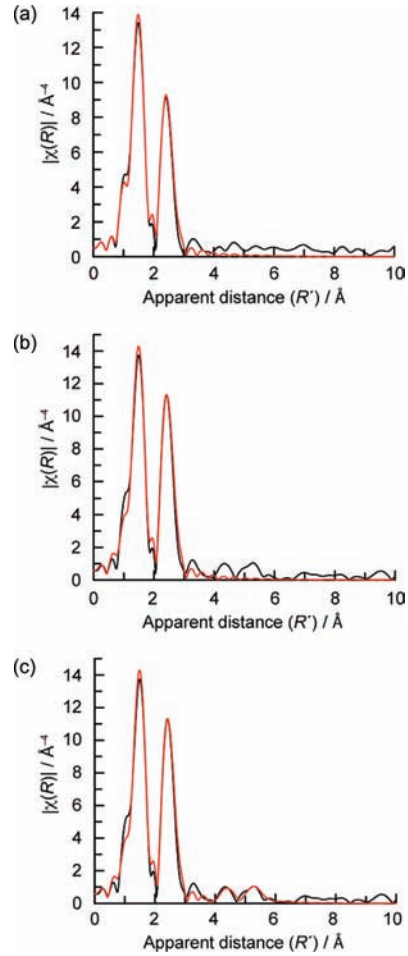

Figure 4. Fits (red) to the Co−Pi EXAFS spectra (black). (a) Fit to surface Co−Pi. (b,c) Respectively, fits 1 and 2 to bulk Co−Pi. Parameters derived from the fits are given in Tables 2 and 3.

(Figure 4a and Table 2). Since the features at $R' > 3$ Å are extremely weak, only features up to $R' = 3$ Å were considered in the curve fitting. As with CoO(OH) and bulk Co−Pi (vide infra), peak I in the FT corresponds to a Co−O vector with $R = 1.89$ Å, and peak II corresponds principally to a Co−Co vector with $R = 2.82$ Å. These distances are consistent with

Table 2. Surface Co−Pi EXAFS Curve-Fitting Parameters[a]

path	R^b	N^b	σ^2 (Å^{-2})^c	ΔE_0 (eV)^b	R_f (%)
CoO(ab)	1.89 (0.008)	6.0 (0.5)	**0.003**	1.1 (1.2)	1.4
CoCo(ac)	2.82 (0.011)	3.4 (0.3)	**0.005**		

[a] Fitting region: $1 \le R$ (Å) ≤ 4; $2.88 \le k$ (Å^{-1}) ≤ 11.73. [b] Values in parentheses are uncertainties. See Supporting Information for details. [c] Bold numbers indicate fixed values. The σ^2 value of the Co−Co vector was fixed to the value obtained from the CoO(OH) curve fitting.

Table 3. Co EXAFS Curve Fitting of Bulk KCoPi and NaCoPi[a]

	fit no.	path	R	N	σ^2 (Å^{-2})^b	ΔE_0 (eV)	χ_ν^2 [c]	R_f (%)
bulk KCo−Pi	1	CoO(ab)	1.89 (0.007)	6.0 (0.4)	**0.003**	2.1 (0.7)	3.8	2.2
		CoCo(ac)	2.82 (0.014)	4.5 (0.6)	**0.005**			
	2	CoO(ab)	1.89 (0.007)	6.0 (0.4)	**0.003**	2.1 (0.7)	3.5	1.7
		CoCo(ac)	2.82 (0.006)	4.5 (0.3)	**0.005**			
		CoCo(af)	4.84 (0.057)	3.1 (3.0)	**0.009**			
		CoCo(ag)[d]	5.69 (0.039)	1.7 (1.3)	**0.004**			
bulk NaCo−Pi		CoO(ab)	1.89 (0.007)	6.1 (0.4)	**0.003**	2.5 (0.7)		2.0
		CoCo(ac)	2.82 (0.007)	4.5 (0.3)	**0.005**			
		CoCo(af)	4.89 (0.050)	3.2 (1.7)	**0.009**			
		CoCo(ag)[d]	5.71 (0.034)	2.7 (0.7)	**0.004**			

[a] Fitting region: $1 \le R$(Å) ≤ 6; $2.88 \le k$(Å^{-1}) ≤ 11.73. [b] Bold numbers indicate fixed values. The σ^2 values of the Co−Co vectors are fixed to the values obtained from the CoO(OH) curve fitting. [c] χ_ν^2 is the reduced χ^2 value. See Supporting Information for details. [d] Multiple scattering path, Co−Co−Co.

Co ions linked by oxo or hydroxo bridges.[31] If N for the Co−O vector is fixed to 6.0, the corresponding σ^2 is found to be 0.003 Å^{-2}. Since 6 is the preferred coordination number for Co^{3+}, we used 0.003 Å^{-2} as a fixed value for this σ^2 in the fitting procedure for both surface and bulk Co−Pi. The σ^2 for the Co−Co vector was fixed to the value obtained from the best fit to the CoO(OH) spectrum (0.005 Å^{-2}). With this value, which we consider to be a reasonable lower limit (vide infra), the best fit for the surface Co−Pi spectrum was obtained with $N = 3.4$. The origin of the peak III feature in the surface Co−Pi spectrum could not be determined by curve fitting because of its very weak intensity.

As with surface Co−Pi, a good fit was obtained for the bulk Co−Pi spectrum by including only two absorber−backscatterer interactions (Figure 4b and Table 3, Fit 1). Peaks I and II correspond to Co−O and Co−Co vectors with $R = 1.89$ Å and 2.82 Å, respectively. However, the N value for the 2.82 Å Co−Co vector is increased to 4.5 for bulk Co−Pi compared to 3.4 for surface Co−Pi with the same fixed value for σ^2 (0.005 Å^{-2}). In addition to a stronger peak II that is reflected in this increased N value, the bulk Co−Pi spectrum has somewhat stronger features at $R' > 4$ Å (peak IV region) relative to the surface Co−Pi spectrum. These features can be fit with additional Co−Co vectors at 4.84 Å and 5.69 (Figure 4c and Table 3, Fit 2). Analogous vectors are required to fit much stronger peak IV features in the CoO(OH) spectrum. The σ^2 values obtained for these vectors in the best fit to the CoO(OH) spectrum were used as fixed values for Fit 2 to the bulk Co−Pi spectrum. There is a small improvement in the overall quality of the fit to the bulk Co−Pi spectrum with the inclusion of the longer Co−Co vectors (Table 3); however, the uncertainties in the N values for these vectors are very large due to the weak intensity of the spectral features in the peak IV region. Nonetheless, the increased N value for the nearest-neighbor Co−Co vector (peak II) and the appearance of spectral features associated with longer Co−Co vectors (peak IV) indicate the presence of larger Co−oxo/hydroxo clusters in bulk Co−Pi relative to surface Co−Pi.

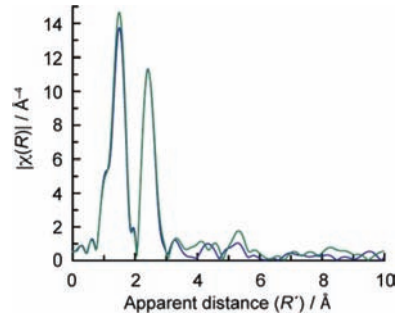

Figure 5. Comparison of FT EXAFS data for bulk Co−Pi prepared from KPi (blue) and NaPi (green).

As in the surface Co−Pi spectrum, the origin of peak III in the bulk Co−Pi spectrum is inconclusive due to its weak intensity. Risch et al. have suggested the possible contribution of a Co−K vector to the corresponding peak III in their ex situ data.[25] However, attempts to incorporate Co−K vectors into the fits for the data here were unsuccessful, leading to substantially increased error values or negligible effects on the fitting quality. To determine the effect of K^+ on the EXAFS spectrum explicitly, a Co−Pi catalyst was prepared under identical conditions to the bulk sample described above with sodium phosphate used in place of potassium phosphate and spectra were collected as described above. The substitution of Na^+ for K^+ does not have a significant effect on Co−Pi activity. A comparison of the FT EXAFS for bulk Co−Pi prepared in KPi (KCo−Pi) and NaPi (NaCo−Pi) electrolyte is shown in Figure 5. The spectrum of Co−Pi prepared with NaPi is similar although not identical to the spectrum of Co−Pi prepared with KPi. The FT of the sample prepared from NaPi shows a slightly higher ratio of peak I to peak II and stronger features for $R' > 3$ Å. The data was fit to four absorber−backscatterer pairs. The structural parameters extracted are similar to those of the sample prepared in KPi (Table 3). Since K^+ is a stronger scatterer than Na^+, peaks that result from a Co−K vector in the FT of the Co−Pi EXAFS data are expected to be reduced upon substitution with Na^+. The stronger features at $R' > 3$ Å in the EXAFS of Co−Pi samples prepared in NaPi are therefore inconsistent with the presence of significant Co−K vectors in the EXAFS of the surface and bulk Co−Pi samples described here.

Discussion

Comparison of the XAS spectra for surface and bulk Co−Pi indicates the presence of the same Co−oxo/hydroxo structural motif in both catalyst samples but different average cluster sizes. The edge shapes are nearly identical for the two samples and the EXAFS spectra contain the same major features. The similarities in the XANES edge position and the EXAFS spectra of the Co−Pi catalysts to those of CoO(OH) suggest that a viable model for Co−Pi may be constructed based on the edge-sharing CoO_6 octahedra structural motif found in cobaltates. We refer to such a model for Co−Pi as a molecular cobaltate cluster (MCC) to denote the molecular dimensions of this structural motif in the Co−Pi samples. This model is described below and compared to an alternative model consisting of corner-sharing cubanes. Structural insight provides a context for interpretation of Co valency according to the XANES data. As described below, the 0.3 eV edge shift at an applied potential of 1.25 V and the more drastic edge differences at OC between bulk and surface Co−Pi highlight an apparent sensitivity of

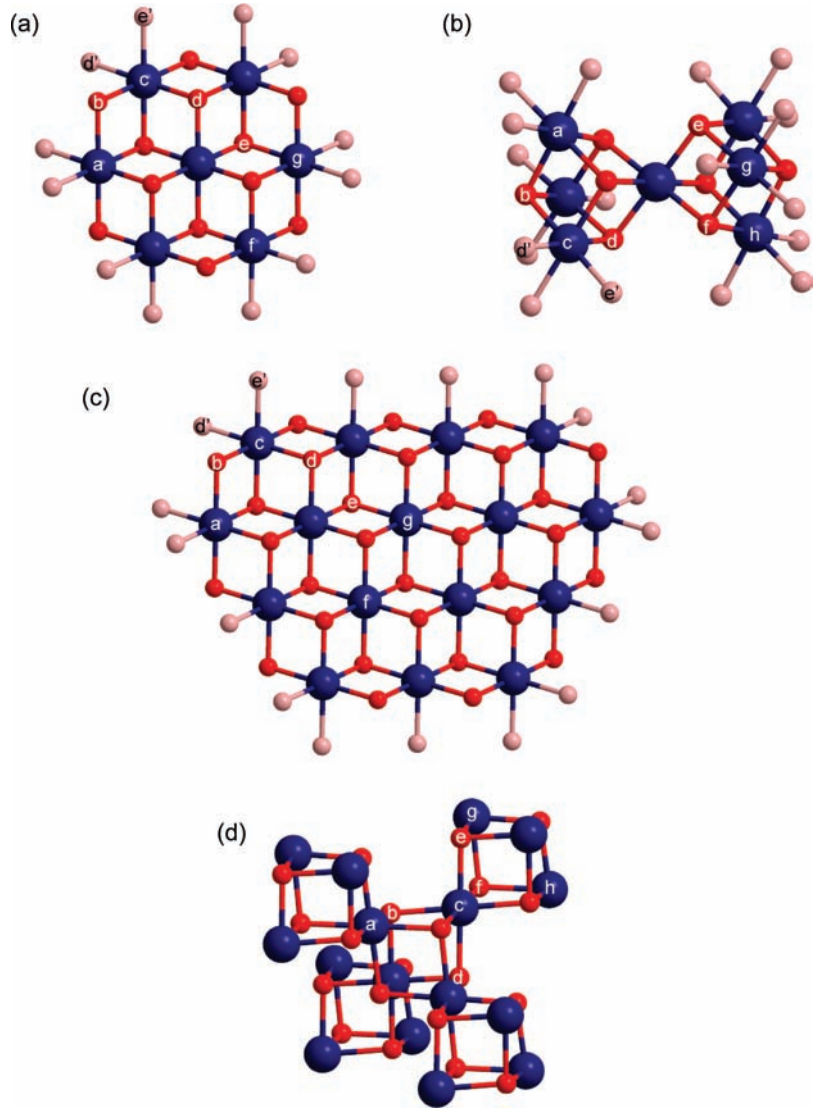

Figure 6. Structural models for Co−Pi. Bridging oxo/hydroxo ligands are shown in red, nonbridging oxygen ligands (including water, hydroxide, and phosphate) complete the octahedral coordination geometry of each peripheral Co ion (blue) and are shown in light red. (a) Edge-sharing molecular cobaltate cluster (MCC) model for surface Co−Pi. (b) Corner-sharing cubane model for surface Co−Pi. (c) Edge-sharing MCC model for bulk Co−Pi. (d) Corner-sharing cubane model for bulk Co−Pi.

valency to cluster size. These results stand in contrast to the stability of high Co valencies in known crystalline cobaltate compounds.

Structural Models for Co−Pi. The first-shell Co−O vector at 1.89 Å and nearest-neighbor Co−Co vector at 2.82 Å derived from the FT EXAFS data are indicative of bis-oxo/hydroxo-bridged Co ions[31] in the Co−Pi samples. The *N* values for the Co−Co vector derived from the best fits, ∼3.4 in surface and ∼4.5 in bulk Co−Pi, indicate that this structural feature is incorporated in higher-order Co−oxo/hydroxo clusters. The difference in cluster sizes (or distributions of sizes) between surface and bulk Co−Pi may simply be a consequence of the difference in the amount of material deposited. Alternatively, the difference in applied potentials used to deposit surface and bulk Co−Pi (1.1 and 1.25 V, respectively) may lead to distinct MCC sizes.

Although it is clear that the *N* value is greater for bulk Co−Pi relative to surface Co−Pi, *N* values are correlated with the σ^2 values and therefore it is difficult to determine absolute values accurately. The *N* values are nonetheless important for discriminating between models for the Co−Pi catalysts. As described below, *N* values ≥4 strongly favor an edge-sharing octahedra model over a corner-sharing cubane model for Co−Pi. To obtain the best fit values above, σ^2 was fixed to the value obtained for the corresponding vector from the best fit to the CoO(OH) spectrum. We considered this σ^2 to be a reasonable lower limit because static disorder is expected to be lower in the crystalline CoO(OH) compound relative to Co−Pi. Larger σ^2 values result in larger *N* values.

The FTs of the EXAFS spectra for the Co−Pi samples exhibit many similarities to the FT of the CoO(OH) spectrum but lack the intense peaks at higher R' values that result from the long-range order in CoO(OH). These results suggest that Co−Pi may consist of Co−oxo/hydroxo clusters composed of edge-sharing CoO_6 octahedra, which are the basic structural components of the extended planes of the CoO(OH) layers shown in Figure 3a and analogous alkali metal cobaltates.[32] A cluster model (MCC) that is consistent with the parameters extracted from the EXAFS data for surface Co−Pi is shown in Figure 6a. All bridging oxo/hydroxo ligands are shown in red and the O atoms

of nonoxo peripheral ligands (e.g., hydroxide, water, phosphate) are shown in light red. The Co_2O_2 units are planar in the edge-sharing CoO_6 octahedra. The MCC model for surface Co−Pi includes a total of 24 nearest-neighbor Co−Co vectors (each linked by two oxos/hydroxos; e.g. path a−c in Figure 6a) and 7 Co ions, corresponding to $N = 3.43$, in accord with the value obtained from the best fit to the EXAFS data ($N = 3.4$, Table 2). The model also includes outer shell Co−Co vectors at 4.89 Å (path a−f) and 5.64 Å (path a−g; multiple scattering path) with N values of 1.71 and 0.86, respectively. These relatively low N values could explain the absence of significant peaks at higher apparent distance in the FT of the surface Co−Pi EXAFS. In contrast, $N = 6$ for the analogous Co−Co vectors in the extended planes of CoO(OH) (Figure 3a) and substantial peaks are discernible in the FT at longer distances (Figure 2).

An alternative model for Co−Pi has been proposed based on EXAFS studies of catalyst films that are frozen immediately after switching from active catalysis to OC conditions.[25] In this study, complete or incomplete corner-sharing Co−oxo cubanes were proposed. A complete corner-sharing Co−oxo cubane model for surface Co−Pi is shown in Figure 6b. All Co ions are linked by two oxo/hydroxo bridges (red) to each neighboring Co and the nonbridging ligands (light red) on the Co ions include oxygens from water, hydroxide, and phosphate. In contrast to the planar units in the edge-sharing CoO_6 octahedra, the Co_2O_2 units in the corner-sharing cubane geometry are puckered, with a Co−O−Co−O dihedral angle of 6.7°. For a model consisting of two corner-sharing complete cubanes with 1.89 Å Co−O and 2.82 Å Co−Co distances, the N values for 2.82 Å (path a−c in Figure 6b), 4.89 Å (path a−g), and 5.64 Å (path a−h) Co−Co vectors are identical to those of the MCC model proposed here for surface Co−Pi (Figure 6a). On the basis of the Co−O vectors at ∼1.89 Å and the Co−Co vectors at ∼2.82 Å, we conclude that both models are consistent with the EXAFS data for surface Co−Pi.

There are longer Co−O vectors >3 Å in both the MCC and corner-sharing models. These vectors may involve either O atoms that form the μ-oxo/hydroxo bridges (red) of the cluster (paths a−d and a−e in Figure 6a; paths a−d, a−e, and a−f in Figure 6b) or peripheral O atoms (light red) that are part of water, hydroxide, or phosphate ligands (paths a−d′ and a−e′ in Figure 6a and b). However, the O−Co−O angles involving peripheral O atoms are likely to deviate from the values found in the Co−oxo/hydroxo cores of each model, resulting in substantial distance heterogeneity for the a−d′ and a−e′ paths. This distance heterogeneity therefore does not require first-shell Co−O distance (1.89 Å) heterogeneity. In addition, the FT peak associated with the a−d path overlaps with the much stronger peak associated with the Co−Co vector in peak II and spectral features at $R' > 3$ Å that are associated with other Co−O paths are of weak intensity. For these reasons, longer Co−O vectors do not provide a reliable basis to discriminate between the MCC and corner-sharing cubane models for surface Co−Pi.

Whereas both models are consistent with the EXAFS spectrum for surface Co−Pi, significant differences between the surface and bulk Co−Pi EXAFS spectra are better accounted for by a MCC model. Specifically, the intensity of the peak corresponding to the nearest-neighbor Co−Co vector in the FT EXAFS of bulk Co−Pi is greater than that of surface Co−Pi. As a result, the N for this vector in the fit to the data increases to 4.5 (Table 3). As noted above, the fixed σ^2 value used for this vector (0.005) is an estimated lower limit, and, if σ^2 is higher, the value of N will also be higher than 4.5. The MCC model can be extended in size to accommodate this increase in N, up to a limiting value of 6.0 found in the extended CoO(OH) structure. As an example, a MCC model including 16 octahedral Co ions that has a total of 68 nearest-neighbor Co−Co vectors, corresponding to $N = 4.25$, is shown in Figure 6c. In contrast, the N value for the nearest-neighbor Co−Co vector cannot exceed 4.0 for a corner-sharing cubane architecture—this value is the limiting value of an infinitely extended framework comprising corner-sharing Co−oxo cubanes. Figure 6d shows an example of an extended corner-sharing cubane motif containing 16 Co ions; here the N value for the 2.82 Å vector is 3.75.

The increase in N for the nearest-neighbor Co−Co vector for bulk Co−Pi relative to surface Co−Pi is accompanied by the appearance of additional weak features in the peak IV region. These features can be fit with longer Co−Co vectors at 4.84 Å and 5.69 Å (Table 3, fit 2). These distances are consistent with the longer Co−Co vectors in both MCC and corner-sharing cubane models (4.89 Å and 5.64 Å, respectively; paths a−f and a−g in Figure 6c and paths a−g and a−h in Figure 6d). As for the nearest-neighbor Co−Co vector, the limiting N value for the ∼5.64 Å Co−Co multiple scattering path differs for the MCC and corner-sharing cubane models ($N = 6.0$ for infinitely extended MCC and 2.0 for infinitely extended corner-sharing cubane). However, the features are too weak and the uncertainties in N values are too large to enable discrimination between the two models on the basis of the longer Co−Co vectors. Thus, the nearest-neighbor Co−Co vector provides the strongest argument based on XAS data for the MCC model over a corner-sharing cubane model.

We also favor a MCC model over a corner-sharing cubane model on the basis of structural data for synthetic Co−oxo compounds. Substantial Co−Co nearest-neighbor distance heterogeneity is observed in single Co−oxo cubanes. For example, cubanes prepared in the presence of carboxylates contain both carboxylate-bridged and nonbridged faces, yielding two sets of Co−Co distances that differ by 0.15−0.2 Å.[33−37] We expect that cubanes formed in the presence of phosphate ions would exhibit similar bridged and nonbridged distance heterogeneity and therefore a decrease of the peak II intensity. Additionally, we note that the edge-sharing CoO_6 octahedral structural motif of the MCC model proposed here is also found in the reduced Co_4O_{16} core of a Co polyoxometallate complex that has recently been reported to effect water oxidation catalysis in the presence of a suitable chemical oxidant.[38]

Other cubane-type models besides the corner-sharing cubanes depicted in Figure 6, b and d, can be ruled out on the basis of the EXAFS data. The absence of a Co−Co vector at ∼3.8 Å in the spectra for the Co−Pi samples rules out models that include approximately linear Co−O−Co vectors. Such models include face-sharing and edge-sharing Co−oxo/hydroxo complete-cubane-type structures, as well as corner-sharing cubanes in which the shared corner is an oxygen atom. This linear arrangement of Co ions would significantly increase the intensity in the peak III region. Face-sharing and edge-sharing cubane-type structures would also necessitate additional nearest-neighbor Co−Co vectors, attenuating the peak II region.

Finally, the MCC model is supported by the recent revision of the Pourbaix diagram of the Co/H_2O system that situates CoO(OH) as the thermodynamically stable species at potentials above ∼0.75 V (vs NHE) in neutral solutions at room temperature.[39] It is feasible that the MCC-type clusters we propose

herein are in fact nuclei of CoO(OH) whose growth is stunted by the presence of phosphate anions during the electrodeposition process.

The MCC models in Figure 6, a and c, are representative clusters with Co−Co *N* values that match the best fit values from the curve fitting. Other MCC clusters with similar *N* values are possible. It is likely that the Co−Pi samples contain a distribution of MCC clusters with an average *N* value that accounts for the intensity of peak II. We also note that MCC clusters may form linkages to each other through bridging oxo, hydroxo, or phosphate moieties. Distinct Co−Co scattering vectors that may arise from these linkages would possess *N* values well below 0.5 and, therefore, contribute negligibly to the EXAFS spectrum. We note that the coexistence of MCC units and corner-sharing cubane units in Co−Pi samples cannot be ruled out, although it is unlikely that the electrodeposition process yields two significantly different structural motifs in comparable quantities. In addition, merging edge-sharing CoO_6 octahedra and cubane motifs into a single structural unit results in substantial nearest-neighbor Co−Co distance heterogeneity and additional Co−Co vectors that are inconsistent with the EXAFS data. For example, forming a cubane on a MCC fragment results in three Co−Co vectors at ∼2.5 Å and two Co−Co vectors at ∼3.8 Å if the Co−O distances are kept at 1.89 Å (Figure S4, Supporting Information).

All attempts to incorporate a Co−P vector into the EXAFS fits for surface and bulk Co−Pi were unsuccessful. The Co:P ratio in Co−Pi samples prepared under similar conditions is between 2:1 and 3:1, as determined by elemental analysis and energy-dispersive X-ray analysis.[18,24] The absence of a Co−P vector may reflect the absence of phosphate−Co binding in Co−Pi. However, coordination of HPO_4^{2-} to the terminal d′ and e′ sites of the outer ring of the cobalt ions is not inconsistent with the EXAFS data. A structurally characterized Co^{3+} complex with a chelating HPO_4^{2-} ligand has recently been reported.[40] If HPO_4^{2-} is bound in this manner in Co−Pi, the *N* value for a Co−P vector would not be in excess of 0.5, a value that would support only a very small signal. Phosphate bound to these sites would likely be highly exchangeable, consistent with ^{32}P radiolabel studies of phosphate exchange within the film. The presence of μ-phosphato ligands would increase the *N* value for a Co−P vector, but if multiple coordination modes for phosphate were present in Co−Pi, large Co−P distance heterogeneity would reduce the signal.

Elemental analyses of Co−Pi catalyst films indicate an approximately 1:1 ratio of K^+ ions to phosphate ions. We speculate that these ions are coordinated to the peripheral ligands of the MCC clusters or to lattice water molecules. Although coordination of K^+ to the Co−oxo cluster cannot be ruled out, there is no evidence that a Co−K vector makes a substantial contribution to the EXAFS spectrum. In addition, replacement of K^+ with Na^+ slightly increases the intensity of peaks in the FT at $R' > 3$ Å, the opposite trend from what would be expected if one of these peaks had a Co−K component.

Cobalt Valency in Co−Pi. Comparison of the peak positions in the Co−Pi edges to that of CoO(OH) suggest a Co valency greater than 3 for Co−Pi when a potential of 1.25 V is applied (Figure 1a). This qualitative assignment is supported by several pieces of independent data. The CV of Co−Pi exhibits an anodic wave as a prefeature to a catalytic wave (Figure S1, Supporting Information). The observed half-wave potential of the prefeature at 0.95 V is in the range of a typical $Co^{2+/3+}$ redox couple; the $Co(OH)_2^{+/0}$ couple is estimated to be 1.1 V[41] and the Pourbaix diagram of cobalt indicates that oxidation of Co_3O_4 to Co(O)OH occurs at ∼0.75 V at pH 7.[39] The $Co^{2+/3+}$ couple for Co−Pi at 0.95 V occurs ∼0.14 V negative of the catalytic wave for water oxidation, consistent with a formal oxidation state of Co^{3+} prior to catalysis. A catalytic wave is obtained only upon further oxidation of the Co^{3+} film. In addition, EPR studies of Co−Pi samples freeze-quenched after deposition at 1.14 V have confirmed the presence of Co^{4+} when the potential is stepped into the range needed for water oxidation.[29]

The first shell Co−O distances and the nearest-neighbor Co−Co distances deduced from EXAFS data (vide supra) also support the assignment of a Co valency greater than 3 by comparison to corresponding distances in alkali cobaltates of various valencies.[32] In the all-Co^{3+} oxides CoO(OH) and $LiCoO_2$, the Co−Co distances are 2.85 Å and 2.81 Å, and the Co−O distances are 1.90 Å and 1.92 Å, respectively. For the series Na_xCoO_2, the corresponding distances range from 2.89 Å and 1.94 Å for $x = 1$ (all Co^{3+}), to 2.81 Å and 1.81 Å for $x = 0.3$ (formally 70% Co^{4+}). The Co−Co distance (2.82 Å) observed for the Co−Pi samples under an applied potential is at the short end of the range of distances observed in cobaltates with valencies greater than 3 and the Co−O distance (1.89 Å) is in the middle of the corresponding range.

The higher-energy edge of bulk Co−Pi vs surface Co−Pi reflects a greater extent of oxidation in the former at 1.25 V (Figure 1b). We attribute this difference to differences in local structure between the two samples. EXAFS data indicate the presence of higher-nuclearity Co oxo structures in bulk Co−Pi (vide supra). We surmise that these larger clusters are able to accommodate more holes per Co than the smaller clusters in surface Co−Pi at a given applied potential. It is not possible to quantify the difference in oxidation state between the two samples on the basis of the XANES data. We note, however, that similar edge shifts have been observed in the XANES spectra of sodium cobaltates (Na_xCoO_2; $x = 0.24-1.0$). Peak positions shift monotonically, although nonlinearly, by a total of 3 eV as the Co valency is increased from 3 to 3.76.[32]

The OCP traces indicate continuous reduction of Co−Pi upon switching from 1.25 V to OC (Figure 1b). As water is the only reductant available, these data indicate residual water oxidation activity by the Co−Pi catalyst. The reduction of the cobalt ions is evident in edge shifts to lower energy in the XANES spectra. The rate of reduction is more rapid for surface Co−Pi than bulk Co−Pi. The edge at OC in the first near-edge scan for bulk Co−Pi almost coincides with the edge of surface Co−Pi at 1.25 V, indicating that the Co valency of bulk Co−Pi is still greater than 3 in the first 10 min after switching to OC. In contrast, the edge of surface Co−Pi is shifted to lower energy by >1 eV and the shape is broadened, indicative of a valency less than 3. We note that the difference in the amount of Co ions in surface vs bulk Co−Pi estimated by electrochemical methods (vide supra) approximately matches the difference in current density observed for the two samples, with both differing by a factor of approximately 15. This consistency suggests that solvent accessibility to active sites is not limiting catalysis at 1.25 V in the thicker bulk sample and therefore should not limit residual water oxidation catalysis at OC. Rather than solvent accessibility, we ascribe the differences in open circuit behavior to structural differences between surface and bulk Co−Pi. At a given average Co valency, the larger clusters in bulk Co−Pi are more stable than those of surface Co−Pi, resulting in slower kinetics for water oxidation. At 1.25 V, the rates of water oxidation per Co ion are comparable for the two samples, but

the valency of bulk Co−Pi is greater. At OC, the decay of OCP and concomitant edge shift for surface Co−Pi are more rapid because the small clusters effect water oxidation at lower Co valencies relative to bulk Co−Pi.

The continual reduction of Co−Pi upon switching to open circuit from 1.25 V is in contrast to the properties of solid-state cobaltate materials. Sodium cobaltates with Co valencies ≥ 3.4 are kinetically stable to water across the pH spectrum.[42−45] This stability is not the result of limited contact between H_2O and the Co ions; H_2O and H_3O^+ molecules readily intercalate between the CoO_2 planes. Evidently, the extended CoO_2 planes in the cobaltates support high Co valencies while remaining resistant to water oxidation. In contrast, the high catalytic activity of Co−Pi suggests that the MCCs promote water oxidation if the Co valency is greater than 3.

Conclusion

The ability to deposit Co−Pi on a variety of conductive surfaces under mild conditions has facilitated the acquisition of X-ray absorption spectra of active catalyst material. The EXAFS spectra indicate that active Co−Pi is composed of bis-μ-oxo/hydroxo-linked Co ions. A comparison of the EXAFS spectra to the spectrum of a cobaltate compound, CoO(OH), support a molecular cobaltate cluster (MCC) model for Co−Pi. In this model, the Co−oxo/hydroxo clusters possess the same structural motif found in the extended planes of cobaltates—edge-sharing CoO_6 octahedra—but have molecular dimensions. In contrast to a corner-sharing biscubane model, the MCC model can accommodate N values for the nearest-neighbor Co−Co vector greater than 4, as seen in the thicker Co−Pi film studied here. The XANES spectra indicate a Co valency greater than 3 during catalysis at an applied potential of 1.25 V and residual water oxidation catalysis at open circuit. This activity is in contrast to cobaltate materials with high Co valencies and suggests that the molecular dimensions of the clusters found in Co−Pi may be essential for catalysis.

The identification of clusters with molecular dimensions formed via electrodeposition as the principal constituents of the water-oxidizing Co−Pi catalyst raises the possibility of preparing mixed-metal oxide clusters to access more efficient catalysts. Encouragingly, other transition metals such as Mn,[46] Ni,[47] and Ru[48] have been shown to occupy Co positions when doped into sodium cobaltate compounds. Since the average cluster size in one of the samples studied here is only seven Co ions, replacing one or more Co ions with alternative metals might alter the oxidation state vs potential profile or the M−O bond strengths, in turn altering the rate of catalysis. Alternatively, it may be possible to access mixed-metal oxide catalysts with light absorption properties that render them active under illumination without an external bias. Finally, in light of the different valencies exhibited by bulk and surface Co−Pi during catalysis and the relative inertness of oxidized cobaltates, it may prove beneficial to further explore the relationship between deposition conditions and cluster size.

Acknowledgment. We thank the Chesonis Foundation for generous financial support. M.W.K. was supported by a Ruth L. Kirschstein NIH Postdoctoral Fellowship. Y.S is supported by a National Science Foundation predoctoral fellowship. J.Y. and V.K.Y were supported by the Director, Office of Science, Office of Basic Energy Sciences (OBES), Division of Chemical Sciences, Geosciences, and Biosciences of the Department of Energy (DOE) under Contract DE-AC02-05CH11231. Part of this work was funded by the Helios Solar Energy Research Center supported by OBES, DOE, under Contract DE-AC02-05CH11231. Synchrotron facilities were provided by the Stanford Synchrotron Radiation Laboratory (SSRL) operated by DOE OBES. The SSRL Biomedical Technology program is supported by NIH, the National Center for Research Resources, and the DOE Office of Biological and Environmental Research. We thank Dr. Yulia Pushkar for help with collection of preliminary data.

Supporting Information Available: This material is available free of charge via the Internet at http://pubs.acs.org.

JA1023767

(46) Chen, Y.-J.; Liu, C.-J.; Wang, J.-S.; Lin, J.-Y.; Sun, C. P.; Huang, S. W.; Lee, J. M.; Chen, J. M.; Lee, J. F.; Liu, D. G.; Yang, H. D. *Phys. Rev. B: Condens. Mater. Phys.* **2007**, *76*, 092501/1−4.
(47) Gayathri, N.; Bharathi, A.; Sastry, V. S.; Sundar, C. S.; Hariharan, Y. *Solid State Commun.* **2006**, *138*, 489–493.
(48) Strobel, P.; Muguerra, H.; Hebert, S.; Pachoud, E.; Colin, C.; Julien, M. *J. Solid State Chem.* **2009**, *182*, 1872–1878.